Journal of Power Sources 227 (2013) 65–71

Contents lists available at SciVerse ScienceDirect

Journal of Power Sources

journal homepage: www.elsevier.com/locate/jpowsour

Structural and comparative electrochemical study of M(II) oxalates, M = Mn, Fe, Co, Ni, Cu, Zn

Maria C. López, J.L. Tirado, C. Pérez Vicente*

Laboratorio de Química Inorgánica, Universidad de Córdoba, Edificio C3, Campus de Rabanales, 14012 Córdoba, Spain

HIGHLIGHTS

- ► Different transition metal oxalates are nanostructured by the reverse micelle method.
- ► Anhydrous oxalates react reversibly with Li combining faradic and capacitive mechanism.
- ► Manganese oxalate shows the highest capacitive contribution and lower voltage.
- ► Iron, cobalt oxalates show the highest reversible capacity.

ARTICLE INFO

Article history:
Received 7 May 2012
Received in revised form
11 July 2012
Accepted 2 August 2012
Available online 17 November 2012

Keywords:
Oxalates
Characterization
Li-ion battery
Anode

ABSTRACT

Several d-block metal oxalates are obtained by using the reverse micelles method, used for the first time as anode material in lithium-ion test cells, and compared with previous results on other systems. Nickel and zinc dihydrate oxalates crystallize in the β-orthorhombic phase, while the manganese compound adopts the α-monoclinic phase and copper oxalate is obtained as a hemihydrate. By heating the hydrates at adequate temperatures, the anhydrous oxalates can be obtained, except for copper, for which oxalate decomposition takes place simultaneously. Although the highest reversible capacities on cycling were previously reported for mixed Fe–Co oxalates, the best capacity retention was obtained for Mn oxalate at 2C rate. For all solids a double layer plus pseudo-capacitive contribution is observed which allows higher capacities than the theoretical values for a simple conversion reaction.

1. Introduction

In recent years, new anode materials have been developed in an effort to make Li-ion batteries competitive in terms of capacity, power density, safety, and production costs for different applications, including portable electronics, electric vehicle, and stationary storage for intermittent energy sources [1,2]. In this context, different transition metal oxysalts possessing an intriguing electrochemistry vs. lithium have been reported [3–6]. Particularly, transition metal oxalates showed attractive performance on cycling as conversion electrode materials. In these solids, the crystalline structure is no longer preserved after the first cycle and there is a large capacity loss after first discharge. However, after the first cycle the capacity retention is good for up to 100 cycles. The capacity in these electrodes is commonly significantly higher than that of graphite: iron oxalate has reversible capacities close to 700 mAh g^{-1} [3], and cobalt oxalate over 900 mAh g^{-1} [4]. Moreover, different contributions to the total capacity of the oxalates are possible: (i) The charge–discharge reactions are full conversion reactions with more than one electron per formula; (ii) a possible reversible formation of an organic layer [7] responsible for the extra capacity observed that it is disappeared on further charges, or (iii) a capacitive effect favored by the mesoporous structure of the particles (because of the dehydration after the synthesis).

Also the method of synthesis plays an important role, resulting in products with different crystallographic structures and texture. Although micro and nanostructured samples showed reversible capacities above 900 mAh g^{-1}, the nanostructured samples showed higher capacity retention and reversible capacity [3]. Transition metal oxalates, such as cobalt oxalate, can be synthesized in a highly dispersed form by the reverse micelles method [3,4]. The goal of this study is to evaluate the performance as electrode material of other d-block metal oxalates (Mn, Ni, Cu, Zn) prepared by using the reverse micelles method, and to compare with previous results on other systems.

* Corresponding author. Tel.: +34 957218637; fax: +34 957218621.
E-mail address: iq3pevic@uco.es (C. Pérez Vicente).

0378-7753/$ – see front matter © 2012 Elsevier B.V. All rights reserved.
http://dx.doi.org/10.1016/j.jpowsour.2012.08.100

2. Experimental

To synthesize the metal oxalates, the method based on the coalescence of different reverse micelles was used. This method allows controlling the particle size as the micelles act as a microreactor where the product is synthesized. Two separate emulsions were prepared using 0.3 M $M(NO_3)_2$ and 0.3 M $(NH_4)_2C_2O_4$ aqueous solutions, with cetyl-trimethylammonium bromide (CTAB) as surfactant, hexanol as cosurfactant, and isooctane as the oil phase. First, the surfactant, cosurfactant and oil phase were mixed under magnetic stirring. After an homogeneous blend was obtained, the aqueous phase was added. After that, both emulsions were mixed and left under magnetic stirring overnight. When the precipitation was completed, the solid was separated from the hydrocarbon phase by centrifugation at 9000 rpm and washed with a 1:1 mixture of chloroform and methanol several times. Then, the product was dried under vacuum at 80 °C in a Buchi glass oven B-580 for 12 h. Usually, this synthesis method yields hydrated oxalates, as shown in XRD patterns (see "results and discussion" section). To obtain the non hydrated compounds, the samples were heated at 200 °C for 6 h under vacuum in a Buchi oven.

The X-ray diffraction (XRD) patterns of the samples were recorded using a Siemens D5000 with Cu Kα radiation and a graphite monochromator. The XRD patterns were recorded from 10° to 60° 2θ, with a step 0.04° and 2 s per step. The TEM images were obtained with a JEOL 2000 instrument working at 200 kV.

Thermogravimetric Analysis and Differential Thermal Analysis were carried out in a SHIMADZU DTG-60AH instrument under air atmosphere and at a heating rate of 3 °C min^{-1}. About 2–3 mg of sample was placed in an aluminum pan and the data were recorded from 30 °C to 550 °C.

For the electrode preparation, 100 mg of blend was obtained by mixing 60 mg of dehydrated metallic oxalate, 30 mg of carbon black and 10 mg of PVDF. These components were crushed in a mortar, and then the powder was poured in a beaker. Some pyrrolidone was added and stirred until homogeneous slurry was obtained. Finally, it was heated at 120 °C until totally dried. About 5 mg of the mixture was extended on the copper foil adding a drop of pyrrolidone, and then dried at 120 °C under vacuum in a Buchi oven for 3 h. Swagelok test cells were assembled inside an MBraun glove box with the prepared electrode (cathode) versus lithium metal foil (anode), using 1 M $LiPF_6$ in a 1:1 weight proportion of EC and DEC electrolyte supported on Whatman glass microfiber papers. The galvanostatic cycling has been carried out at 1C, 2C and 5C rate (C = 1 Li h^{-1} mol^{-1}). The potentiostatic experiments have been carried out at 0.5, 2, 5, 10 and 20 mV s^{-1} cycling between 0 and 3 V. The instrument used was a multi-channel microprocessor controlled system VMP (a research-grade multi-channel potentiostat from BioLogic Science Instruments).

3. Results and discussion

3.1. Structural/textural characterization of raw oxalates

Dihydrate first-row transition metal oxalates appear in different structures: orthorhombic and monoclinic. Previous studies [3–6] showed that the synthesis method can affect the structure of the obtained product. By direct precipitation method the obtained compounds usually show a monoclinic structure, whereas when the precipitation is carried out inside a restricted volume (as in the case of reverse micelles method) the orthorhombic structure is obtained in most cases.

Fig. 1 shows XRD patterns obtained for synthesized oxalates and the peak indexation according to their correspondent space groups. For dihydrate oxalates $MC_2O_4{\cdot}2H_2O$ with M = Fe, Co, Ni, Zn and mixed $Mn_{0.1}Fe_{0.7}Co_{0.2}$, we obtained the β orthorhombic phase with space group Cccm [8]. On the other hand, in the case of M = Mn we obtained the α monoclinic form with space group C2/c [9]. Finally, for copper oxalate we obtained the hemihydrate oxalate $CuC_2O_4{\cdot}½H_2O$ instead of dihydrate, showing a Pmnn orthorhombic structure. All obtained hydrate metal oxalates are pure, except Zn oxalate, which presents a mixture of hydrate and anhydrous (marked with * in Fig. 1) phases [10]. The refined cell parameters are shown in Table 1.

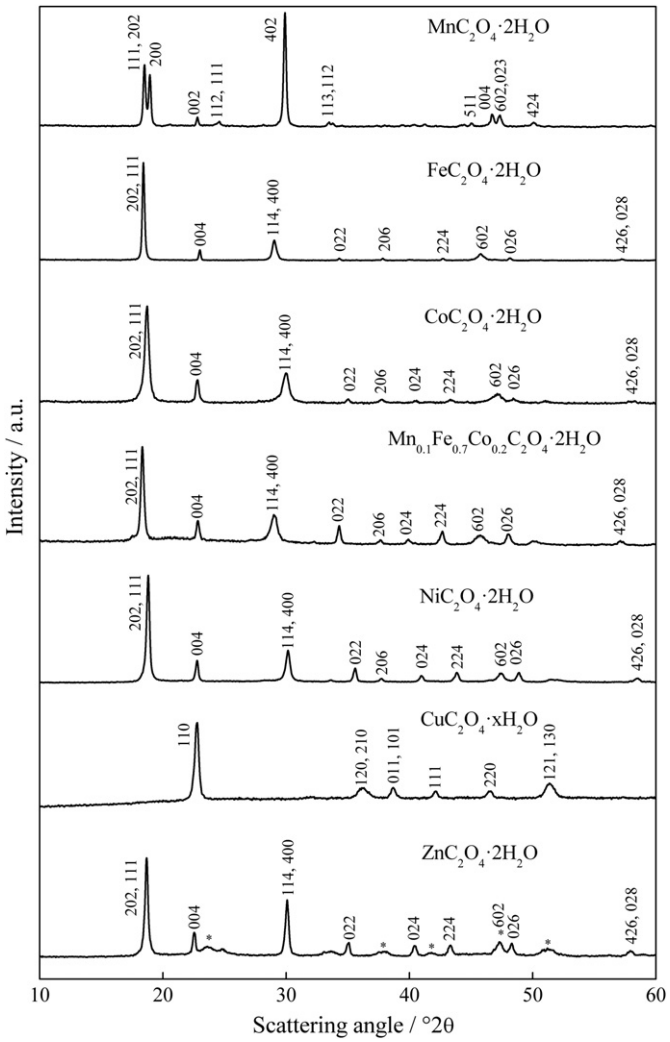

Fig. 1. X-ray diffraction pattern of oxalates obtained by reverse micelle method. The peaks marked with * correspond to anhydrous ZnC_2O_4 traces. The reflections are indexed according to their respective space group: Cccm for Fe, Co, Ni, Zn; C2/c for Mn and Pnnm for Cu.

For the study of thermal behavior, TGA and DTA techniques were used. For dihydrate oxalates, the weight loss takes place in two steps, as shown in Fig. 2 for M = Mn. Similar results were obtained for all dihydrated oxalates. The first step is accompanied by an endothermic peak in DTA. It can be assigned to a loss of crystallization water following the reaction:

$$MC_2O_4{\cdot}2H_2O\ (s) \rightarrow MC_2O_4\ (s) + 2H_2O\ (g) \quad (1)$$

This weight loss is in the temperature range of 100–200 °C. Experimental and calculated weight losses are included in Table 2, as well as the temperature corresponding to the peaks appearing in the DTA curves. The DTA peak for zinc oxalate (109 °C), is close to the temperature used to dry the sample (80 °C). During

Table 1
Refined unit cell parameters. M and *x* are the transition metal and water content, respectively, in the oxalate formula $MC_2O_4 \cdot xH_2O$.

M	*x*	Space group	*a*/Å	*b*/Å	*c*/Å	*β*/°
Mn	2	C2/c	11.96(2)	5.706(6)	9.95(2)	128.48°(2)
Fe	2	Cccm	12.305(3)	5.553(2)	15.464(5)	
Co	2	Cccm	11.90(1)	5.420(5)	15.60(2)	
$Mn_{0.1}Fe_{0.7}Co_{0.2}$	2	Cccm	12.24(3)	5.542(8)	15.55(3)	
Ni	2	Cccm	11.876(6)	5.339(2)	15.659(7)	
Cu	0.5	Pmnn	5.49(1)	5.56(1)	2.565(3)	
Zn	2	Cccm	11.84(3)	5.34(1)	15.66(8)	

drying, the sample was probably partially dehydrated, giving rise to traces of the dehydrated sample ZnC_2O_4, that can be observed in the XRD pattern in Fig. 1 (marked with *).

There is a second weight loss step larger than the first one at temperatures higher than 200 °C for all the samples (as example, see Fig. 2). This step is assigned to the decomposition of the oxalate anion, the products involved in the reaction being CO, CO_2 and MO_x, depending on experimental conditions, as discussed below. The only sample that did not present two steps in the TGA curve was the hemihydrate copper oxalate, whose dehydration and decomposition take place at the same time, having thus only one weight loss, as shown in Fig. 2. In this case, the final product of the heating was CuO, as XRD pattern indicated (not shown).

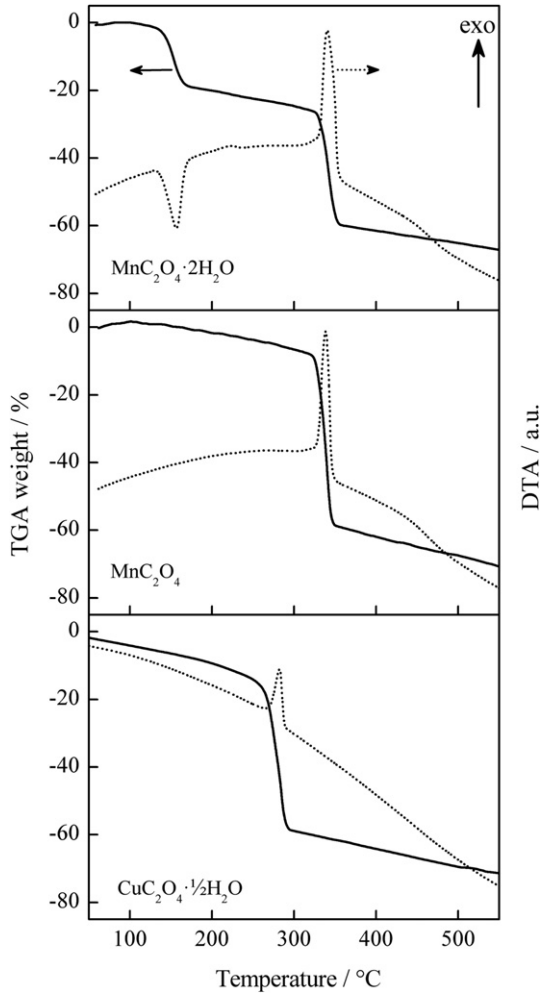

Fig. 2. TGA and DTA curves of selected samples.

Table 2
DTA temperature peak and weight loss of the first step in DTA/TGA curves of dihydrate oxalates $MC_2O_4 \cdot 2H_2O$.

M	DTA peak	Weight loss (%)	
		Experimental	Theoretical
Mn	152 °C	18.5	20.1
Fe	162 °C	21.4	20.0
Co	140 °C	17.6	19.7
$Mn_{0.1}Fe_{0.7}Co_{0.2}$	166 °C	20.5	20.0
Ni	182 °C	18.1	19.7
Zn	109 °C	15.1	19.0

The decomposition step of the oxalate anion took place in the range 210–380 °C depending on the nature of the metal. The decomposition temperature and final oxide products also depend on the atmosphere conditions. Under inert atmosphere the decomposition reaction can be either Equation (2) or (3), depending on the standard free energy of formation of metal oxide from the metal, and carbon dioxide from carbon monoxide.

$$MC_2O_4 \rightarrow M + 2CO_2 \quad (2)$$

$$MC_2O_4 \rightarrow MO + CO + CO_2 \quad (3)$$

If the standard free energy of formation of the metal oxide is lower than that of CO_2 formation from CO, then the oxidation of CO to CO_2 will take place and metallic particles will remain. According to Ellingham diagram, this is the case of Ni and Co. For Mn, Cu and Zn the metal oxide is formed. Iron case is different; the free energy of the iron oxide formation from the metal is very close to that of the formation of carbon dioxide from carbon monoxide. Thus, either metallic particles or iron oxide can be formed. If the atmosphere is air or oxygen, the metallic particles will be oxidized giving rise in all cases metal oxides.

Thus, in the decomposition process of dehydrated metallic oxalate, there are two phenomena of different nature:

- Decomposition (of oxalate anion): the metal oxalate undergoes an endothermic reaction.
- Oxidation (of metal or carbon monoxide): exothermic reaction due to the presence of oxygen during the DTA experiment.

Since both phenomena can occur at the same time, we can only see the influence of the oxidation peak (exothermic) in the DTA experiment, having a contribution much higher than the endothermic effect of the decomposition.

All the samples were heated at 200 °C during 6 h under continuous vacuum to remove the crystallization water, except copper oxalate sample (heated at 240 °C). After that, new TGA experiments were repeated on the heated samples to confirm the water loss and that no decomposition of oxalate took place. For all the samples the water loss step disappeared (except for copper oxalate because both steps occur at the same time) and only the second step (decomposition of oxalate) remained. As example, the case of $MnC_2O_4 \cdot 2H_2O$ is illustrated in Fig. 2-top (before heating at 200 °C) and Fig. 2-middle (after heating).

In Fig. 3 we can see the XRD patterns of the samples after heating at the selected temperatures. The crystallographic structure changes after the heating process for manganese oxalate, from monoclinic to orthorhombic (Pmna space group). For copper oxalate, since the heating temperature is below the decomposition and dehydration temperature, it keeps the same structure (orthorhombic with space group Pnnm). For the other metal oxalates, XRD patterns seem to indicate that the dehydrated oxalates have a similar structure. The patterns are characterized by a loss of

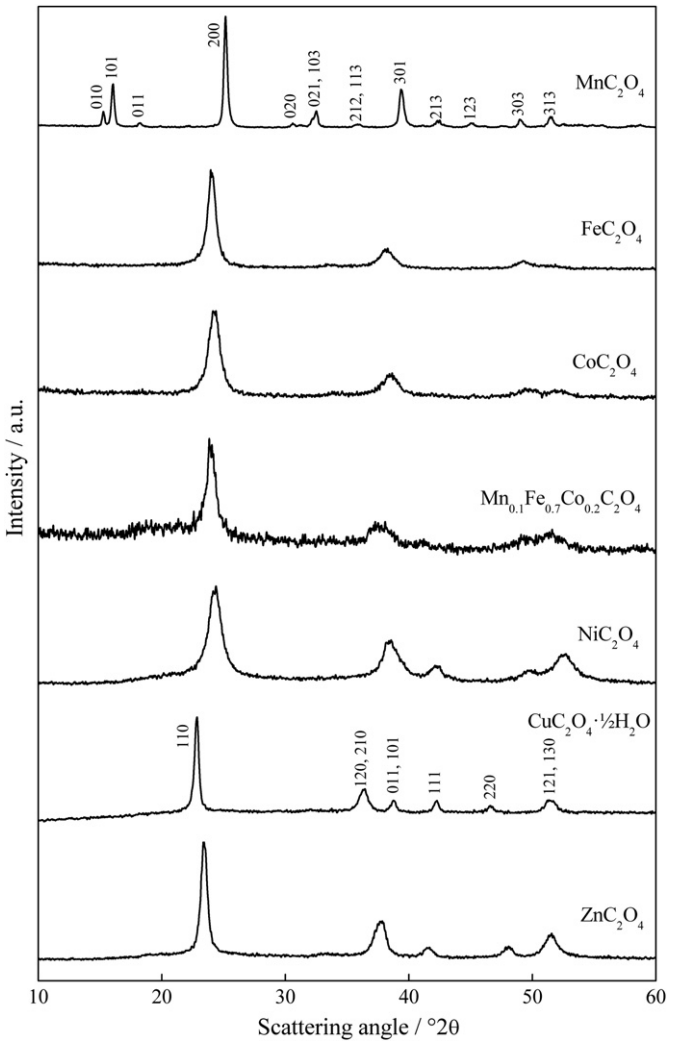

Fig. 3. X-ray diffraction pattern after heating the metallic oxalates at 200 °C, except $CuC_2O_4 \cdot xH_2O$, heated at 240 °C.

reflections and high broadened peaks, which agree with poor crystallization of the solid. Brown et al. [8] and Robin [9] also reported a study of the dehydration of ferrous oxalate. The peak positions they reported agree with those of our XRD pattern.

Fig. 4 shows some selected TEM pictures. All samples present particles with a nanoribbon shape, with a width at the nanoscale (in the range from 20 nm for copper and the mixed metal oxalate up to 200 nm, in the case of manganese and zinc) and lengths from 0.2 up to 2 μm. These obtained shapes are similar to previously published results concerning Mn [11], Fe [3], Co [4], and mixed Fe_xCo_{1-x} [6] oxalates. All the samples showed a porous-like texture, similar to that shown in Fig. 4-middle for manganese oxalate. This porous texture is probably due to the water loss taking place during the heating process carried out at 200 °C. Measurements of BET specific surface areas for all initial samples gave values of ca. 30 $m^2\ g^{-1}$, independent of the nature of the cations, the difference between samples being within the experimental error range.

Fig. 4-bottom shows a TEM image of Ni oxalate at high magnification. The Fourier transform of the original image is also shown, where some spots are visible. These spots correspond to an interplanar distance of 2.3 Å, and assigned to the peak below 40° in the XRD pattern shown in Fig. 3. The interferences are clearly visible in the reconstructed image, after applying a high frequency filter to the Fourier transform.

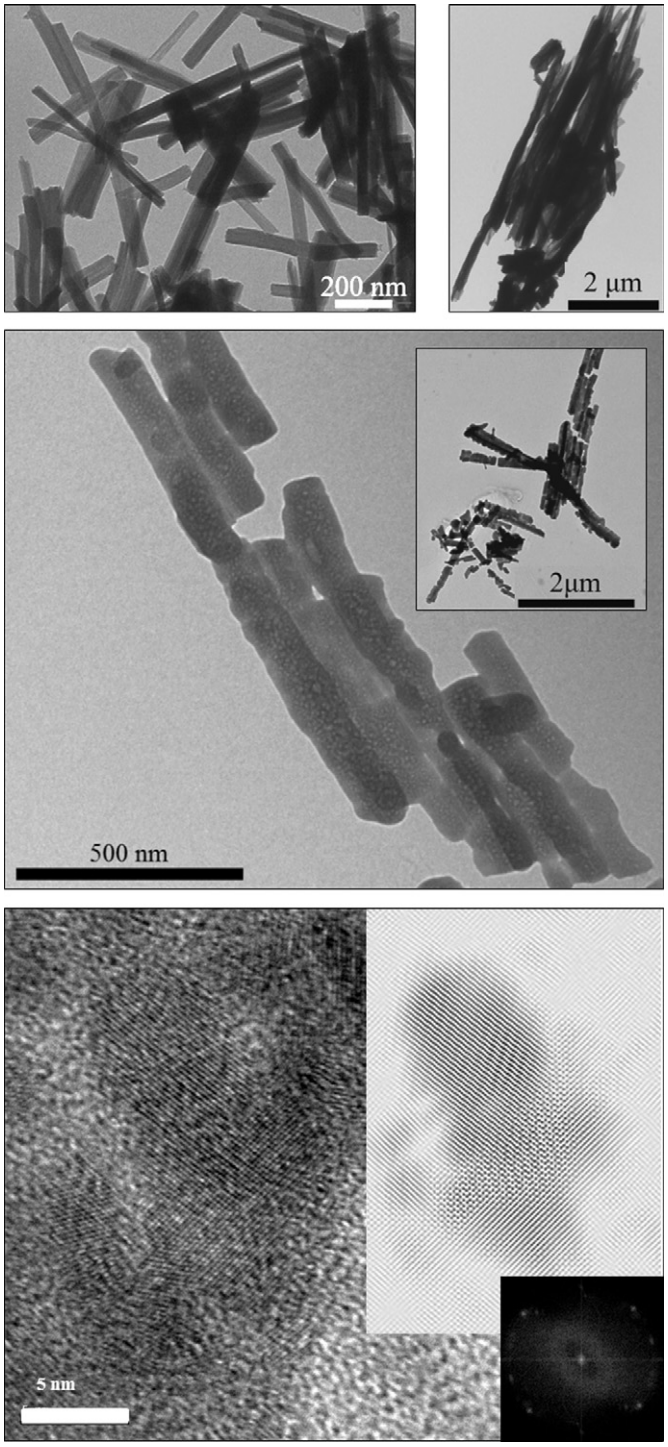

Fig. 4. TEM images of nickel oxalate (top left), zinc oxalate (top right), manganese oxalate, showing the porous texture (middle), and nickel oxalate (bottom) showing the Fourier transform and the reconstructed image after a high frequency filter.

Attempts to observe the particles of the hydrate oxalates, without porous texture, were unsuccessful. We took TEM images of a hydrate zinc oxalate sample. The obtained images looked the same as the dehydrated oxalate, most probably because dehydration occurred on the vacuum chamber in the TEM instrument. To confirm this hypothesis, we introduced a sample of hydrate zinc oxalate in a vacuum chamber at 10^{-7} mbar for 2 h Fig. 5 shows the XRD pattern of this sample, as well as the hydrated and non hydrated phases for its comparison. It can be seen that a partial

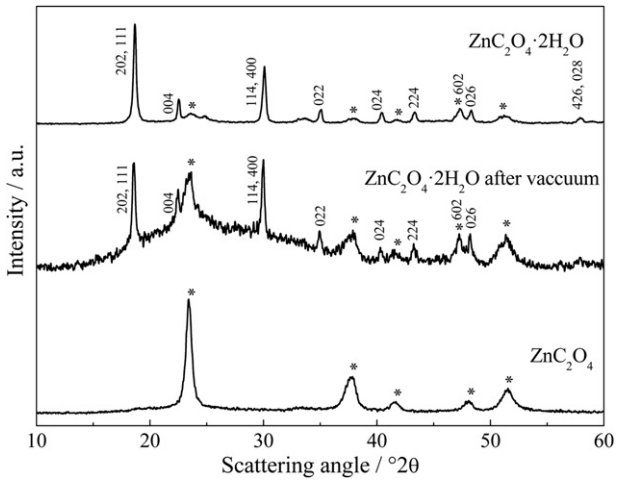

Fig. 5. XRD pattern of hydrated zinc oxalate (top), hydrated zinc oxalate after 10^{-7} mbar vacuum for 2 h (middle) and dehydrated zinc oxalate sample (bottom).

water loss is produced, since the XRD pattern shows the presence of both phases. For this sample only vacuum was applied. In the case of TEM samples, also an electron bombardment was used. This additional factor can contribute to increase the temperature of the sample and the dehydration process can be more important.

3.2. Electrochemical characterization

Fig. 6 shows some selected charge/discharge cycles for different samples (Mn, Ni, Cu and Zn) at 2C rate. The galvanostatic charge/discharge cycling profile is characterized for all the samples by a high capacity value for the 1st cycle with a straight drop down to 0.5–0.7 V for Mn and Zn and 1.4–1.6 V for Ni and Cu. After that, there is a plateau (excepting for Cu), that smoothly decreases down to 0 V (end of discharge) reaching capacity values greater than 1000 mAh g^{-1}. These values are much higher than those theoretically expected for these compounds based on a simple conversion mechanism according to the reaction:

$$MC_2O_4 + 2Li \rightarrow M + Li_2C_2O_4 \quad (4)$$

which capacity values are in the range 350–375 mAh g^{-1} from Zn to Mn, respectively.

On charge for 1st cycle, the voltage rise up rapidly up to ca. 1 V for all the samples. Then, there is a narrow plateau extending up to 400 mAh g^{-1} depending on the sample, and finally rising up rapidly, up to 3 V (upper limit in the voltage window for cycling), evidencing a huge capacity loss (irreversible) in this first cycle. On further cycling (5th, 20th, 80th cycle) the profiles are getting smoother, the plateaus disappear and the capacity values decrease.

Fig. 7 shows the capacity values of MC_2O_4 with M = Mn, Fe, Co, Ni, Cu and Zn at different rates. There are common features for all the studied oxalates: the first discharge capacity is high, and there is also a high irreversible capacity in the first cycles. This large irreversible capacity on the first cycle (due to side reactions; i.e. electrolyte decomposition/oxidation, accompanied by the formation of a solid electrolyte interface) represents ca. 60% of the first discharge, although its contribution can be neglected after 5 cycles. But this is not a major drawback. An adequate previous treatment of the electrode could reduce it. Thus, a recent report [12] shows that, in the case of Sn/C-based materials this irreversible capacity can be decreased from 63% down to 14% by simply contact of the electrode with a wet Li foil for 3 h.

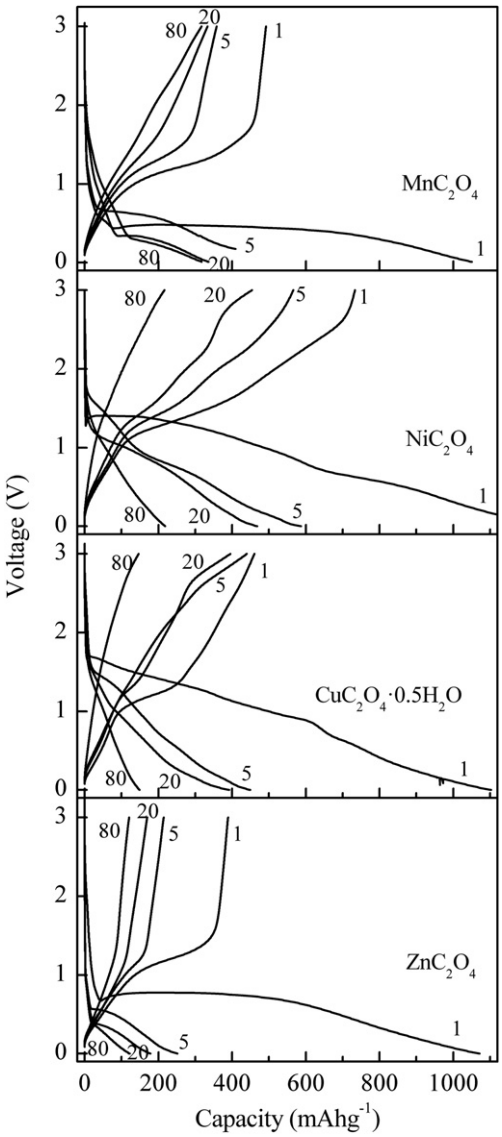

Fig. 6. Selected galvanostatic charge–discharge cycles at 2C rate of lithium test cells using different oxalates as active electrode material.

For nickel oxalate we got the highest initial capacities, but it rapidly drops, reaching a stable reversible capacity of 230 mAh g^{-1} after 60 cycles. In the case of Mn oxalate, although the capacity values decrease at the beginning, after 10 cycles it shows a light recovery of the capacity up to 250 mAh g^{-1}, kept during 100 cycles. Although the capacity values are low, the capacity retention is excellent. As in other conversion systems, an important factor in the degradation of the electrode on cycling is the marked volume changes from the reduced solids after discharge and the oxidized delithiated products. In the case of oxalates, we have carried out the calculation of relative volume changes by using the specific weights of the crystalline phases M, MC_2O_4 and $Li_2C_2O_4$, and found values around 30%, except for MnC_2O_4, in which the variation is ca. 4% due to the different structure of the anhydrous oxalate. This is in good correspondence with the better capacity retention of MnC_2O_4 (Fig. 7 and 2C rate). In the case of Cu oxalate, after the initial capacity drop, it experiments a recovery after 15 cycles, but it starts to decrease again after 20 cycles. For Zn oxalate both capacity values and capacity retention on cycling are poor. The best capacity values on cycling are those of cobalt oxalate and iron oxalate

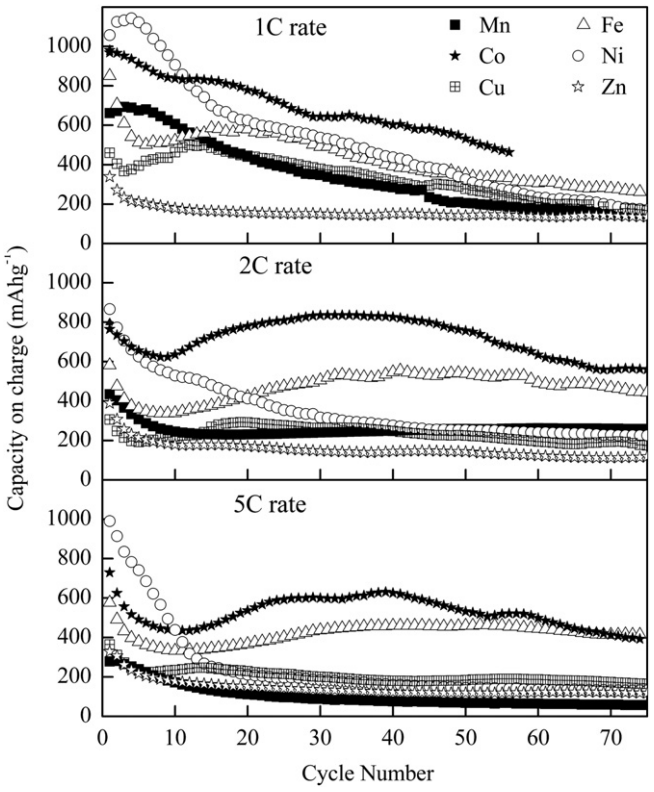

Fig. 7. Reversible capacity on charge upon cycling at different rates of lithium test cells using different oxalates as active electrode material.

reaching maximum values at 2C rate of 800 mAh g^{-1} and 550 mAh g^{-1}, respectively [3,4]. For the rest of oxalates, capacity values are considerably lower at 2C rate, and specially at 5C rate. Mixed Fe and Co oxalates have been studied previously, and the best capacity values were obtained for the mixture $Fe_{0.75}Co_{0.25}$ at 1C rate, achieving values of capacity over 800 mAh g^{-1} for more than 70 cycles [6]. At the light of the high capacity values obtained for Fe–Co mixed oxalates and the excellent capacity retention of Mn oxalate at 2C rate, we decided to introduce small amounts of Mn on Fe–Co mixed oxalates. Thus the sample $Mn_{0.1}Fe_{0.7}Co_{0.2}C_2O_4$ was also studied. The results of this new mixed metal (not shown) are not as good as one could expect. Although during the first 15 cycles the reversible capacity is very good, higher than for the other oxalates, with capacity values higher than 700 mAh g^{-1} at 2C rate up to 20 cycles, then it progressively falls down. The addition of Mn makes the capacity retention to decrease, as compared with the mixed oxalate without manganese, $Fe_{0.75}Co_{0.25}C_2O_4$. The capacity drops progressively down to 250 mAh g^{-1} after 100 cycles, a capacity value close of that of pure Mn oxalate. Thus, the presence of manganese has not synergic effect at all when introduced in a mixed iron, cobalt oxalate $Fe_{0.75}Co_{0.25}C_2O_4$.

Fig. 8 shows the first cycle of cyclic voltammetry at different rates. We can observe the influence of the voltage sweep rate on the voltammograms of different metal oxalates. The reduction peak is below 1.2 V in all cases. On increasing the voltage sweep rate, the reduction peak shifts to lower voltages, as expected, since an increase on the voltage sweep rate favors an increase on the cell polarization. In fact, only nickel oxalate shows clearly the reduction peak at values higher than 0 V. Another similar effect occurs on changing the metal ion. The cation reduction peak shifts depending on the metal ion, having the lowest reduction voltage for Mn and the highest for Cu from among the studied oxalates. The position of the reduction peak in Fig. 8 follows the same sequence than the standard reduction potentials

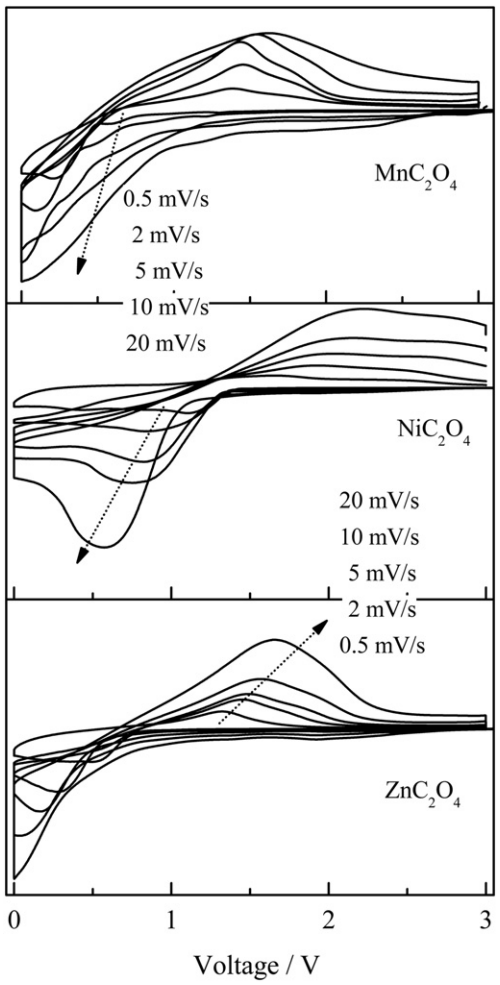

Fig. 8. First voltammetric cycle recorded at variable scan rate of lithium test cells using different oxalates as active electrode material.

of the M^{2+}/M pair in aqueous medium, except for Zn. In fact, its reduction voltage in the electrochemical Li cells can be affected by the possible formation of the lithium-zinc alloy LiZn.

Finally, cycle number also affects cell polarization, and consequently the reduction peak. The first cycle is always different to the following cycles, probably indicating that the original material is not preserved on cycling.

The charge stored in a battery has two components: faradaic and capacitive. The faradaic component is due to two different processes:

- Lithium insertion process.
- Charge transfer with surface atoms.

The latter is linked to inseparable capacitive effects: the double layer effect (capacitive contribution) and the pseudocapacitive contribution from surface conversion reactions [13]. The faradaic current is proportional to the square root of voltage sweep rate, while the capacitive current is proportional to the voltage sweep rate. Thus, capacitive and faradaic contribution can be separated by using Equation (5) [13]:

$$i(V) = k_1 \cdot v + k_2 \cdot v^{1/2} \quad (5)$$

where $k_1 \cdot v$ corresponds to surface capacitive effects and $k_2 \cdot v^{1/2}$ corresponds to diffusion controlled insertion processes and $i(V)$ is

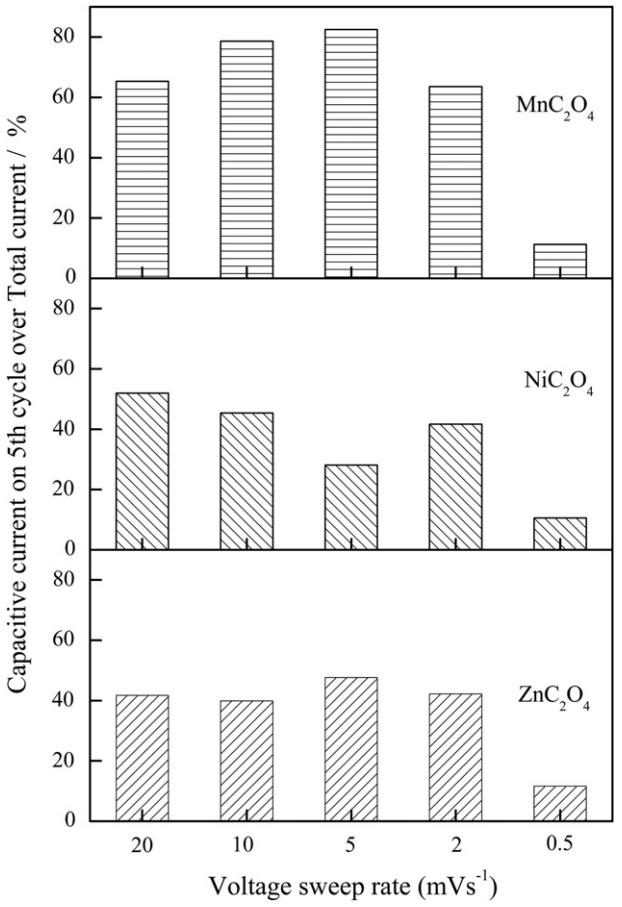

Fig. 9. Capacitive (double-layer plus pseudocapacitive) percentage contributions to the total capacity of oxalate electrodes at different sweep rates.

the current as a function of voltage. Dividing Equation (5) by $v^{1/2}$ we get a straight line with k_1 as slope and k_2 as intercept of Y axis. Thus, we can calculate k_1 and k_2 and, consequently, the capacitive and faradaic current intensities separately.

By this method, faradaic and capacitive contributions have been calculated, and the capacitive current contribution is shown in Fig. 9 for the 5th cycle. The general trend is the higher the voltage sweep rate the higher the capacitive current. For 0.5 mV s^{-1} the capacitive contribution in all cases is less than 50%. Zn and Ni oxalates shows capacitive currents lower than 50% in all cases, whereas in the case of Mn oxalate, the capacitive current is even higher than 70% for all cases except at 0.5 mV s^{-1}. Thus, although a part of the capacitive component of the total capacity could be related to the porous system of the particles, the observed differences between samples (specially for manganese) are not justified simply by taking into account the specific surface, that is the same for all samples. This difference in behavior can be attributed to the fact that the Mn^{2+}/Mn pair is considerably lower than for the other cations, and the reduction is not completed at this rate, thus increasing the relative contribution of the capacitive effect.

4. Conclusions

The reverse micelles method is useful to synthesize d-block metal oxalates with nanoscale particles and crystallization water. Most of them are dihydrated, except for copper which is hemihydrated. Most of dihydrate oxalates crystallize in the β orthorhombic phase, except Mn which adopts the α monoclinic phase. The thermal analysis of hydrate oxalates shows two weight losses: the first one is assigned to the dehydration, while the second corresponds to the oxalate decomposition. Heating the samples at adequate temperatures, the anhydrous oxalate can be obtained, except for copper oxalate, for which both steps take place simultaneously. These anhydrous oxalates present less and broader reflections in the XRD pattern. In the light of TEM images, all the synthesized metal oxalates present nanoribbon shape of particles, with a width at the nanoscale and lengths up to 2 μm, and with porous texture, probably, due to the dehydration process.

Galvanostatic experiments showed for all the studied oxalates that the initial capacity largely excess the expected value based on a simple conversion mechanism, although the reversible capacity decreases upon cycling. The potentiostatic discharge/charge cycles show a reduction peak in the range 1 to 0 V. The reduction peak position shifts to lower voltage values at higher sweep rates. It also shifts depending on the cation present in the metal oxalate. For all the studied oxalates, the first cycle is different to the following cycles. The main contribution to capacity at low discharge sweep rates is faradaic, but it also depends on the cation present in the metal oxalate. From the studied oxalates, the highest capacitive contribution is for Mn. This fact can be attributed to the low voltage value of the reduction pair Mn^{2+}/Mn.

Finally, despite the good capacity retention of some oxalates, more work should be developed to improve their electrochemical performances. At present, the high cut-off voltage, the high irreversible capacity on the first cycle and the difficulties associated for obtaining a 100% free-of-water materials, strongly limit their practical use in lithium batteries.

Acknowledgment

The authors thank MICINN-MEC (MAT2011-22753) and Junta de Andalucía (FQM288) for financial support. MCL thanks the EC for an Erasmus Mundus grant.

References

[1] M. Broussely, in: M. Broussely, G. Pistoia (Eds.), Industrial Applications of Batteries. From Cars to Aerospace and Energy Storage, Elsevier B.V., 2007, p. 244.
[2] X. Yuan, H. Liu, J. Zhang (Eds.), Lithium-Ion Batteries, CRC Press, NY, 2012.
[3] M.J. Aragón, B. León, C. Pérez Vicente, J.L. Tirado, Inorg. Chem. 47 (2008) 10366.
[4] M.J. Aragón, B. León, C. Pérez Vicente, J.L. Tirado, A.V. Chadwick, A. Berko, S.Y. Beh, Chem. Mater. 21 (2009) 1834.
[5] M.J. Aragón, B. León, C. Pérez Vicente, J.L. Tirado, J. Power Sources 189 (2009) 823.
[6] M.J. Aragón, B. León, T. Serrano, C. Pérez Vicente, J.L. Tirado, J. Mater. Chem. 21 (2011) 10102.
[7] A. Débart, L. Dupont, P. Poizot, J.-B. Leriche, J.M. Tarascon, J. Electrochem. Soc. 148 (2001) A1266.
[8] R.A. Brown, S.C. Bevant, J. Inorg. Nucl. Chem. 28 (1966) 387.
[9] J. Robin, Bull. Soc. Chem. 84 (1953) 1078.
[10] A. Kolezynski, A. Malecki, J. Therm. Anal. Calorim. 96 (2009) 645.
[11] T. Ahmad, K.V. Ramanujachary, S.E. Lofland, A.K. Ganguli, J. Mater. Chem. 14 (2004) 3406.
[12] J. Hassoun, K.S. Lee, Y.K. Soon, B. Scrosati, J. Am. Chem. Soc. 133 (2011) 3139.
[13] T. Brezesinki, J. Wang, J. Polleux, B. Dunn, S.H. Tolbert, J. Am. Chem. Soc. 131 (2009) 1802.